

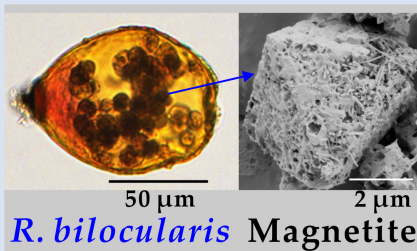
Magnetic foraminifera thrive in the Mariana Trench

H. Yang^{1,2}, X. Peng^{1*}, A.J. Gooday^{3,4}, B. Jones⁵, J. Li¹, S. Liu⁶, W. Huang⁷, Z. Sun⁸,
S. Chen¹, S. Dasgupta¹, H. Xu¹, S. Liu¹, W. Xu¹, K. Ta¹



<https://doi.org/10.7185/geochemlet.2212>

Abstract



R. bilocularis Magnetite

Unicellular magnetic microorganisms include magnetotactic bacteria and some protist species. Although magnetosome magnetite in bacteria (prokaryotes) is well studied, little is known regarding the characteristics and origin of magnetic minerals in protists (eukaryotes). Stercomata stored within tests of the hadal foraminifera *R. bilocularis* from the Mariana Trench (6980–10,911 m depth), contain magnetite crystals. As a result, this species can orient in accordance with magnetic fields. The magnetite differs chemically and physically from that in the surrounding sediments. The crystals also differ from bacterial magnetosomes in being of variable size, porous structure, not arranged in chains, and encapsulated in a lipid membrane. Putting available evidence together indicates a biological origin of the magnetite, although a sedimentary

source cannot be eliminated. This is the first record of a magnetic protist from hadal depths, opening a new window for the biomagnetism in the Earth's extreme environment.

Received 24 November 2021 | Accepted 25 March 2022 | Published 20 April 2022

Introduction

Biogenic magnetite occurs inside magnetotactic bacteria (Mann *et al.*, 1984) and some protists (algae and protozoa) (Bazylinski *et al.*, 2012; Leão *et al.*, 2020; Monteil and Lefevre, 2020), the latter including a number of biflagellates, dinoflagellates, and ciliates, as well as multicellular animals (insects, molluscs, fish, birds, and mammals) (Frankel, 1984; Kirschvink *et al.*, 2001). In these organisms, magnetite facilitates magnetic field detection, making it possible for them to orientate and navigate (Maugh, 1982; Andrews *et al.*, 2003). Bacteria and protists are particularly important in this regard, because their simple structure and wide distribution in various aquatic environments facilitates the study of biogenic magnetite formation and magnetotaxis (Bazylinski and Frankel, 2004; Bazylinski *et al.*, 2012; Leão *et al.*, 2020). Although the synthesis of magnetite nanoparticles in magnetotactic bacteria is well studied (Uebe and Schüler, 2016), the formation mechanisms of magnetite and its physiological functions in eukaryotic protists remain largely unknown.

Several protistan taxa, including diplomonads, kinetoplastids, ciliates, and foraminifera (Todo *et al.*, 2005; Schoenle *et al.*, 2021), have been reported from abyssal plains and hadal trenches, where they probably play a critical role in carbon cycling (Schoenle *et al.*, 2021). Foraminifera are among the most

common meiofauna-sized organisms at hadal depths greater than 6000 m. Between 2016 and 2019, exploration by the R/V TANSUOYIHAO (Table S-1) at 11 stations in the southern Mariana Trench at water depths between 6980 and 10,911 m, recovered numerous specimens of the organic walled species *R. bilocularis* from the surface sediments. This species, which had been described earlier from the Mariana Trench (Gooday *et al.*, 2008) and is currently classified within the foraminiferal class Monothalamina ('monothalamids'), was found to be highly magnetic (Fig. 1a,b).

Results

Response of foraminifera to magnetic fields. All *R. bilocularis* specimens in a sample of 1000 observed in this study showed varying degrees of passive response to the applied magnetic field (Video S-1). A magnetite enrichment experiment based on 1000 *R. bilocularis* showed that each specimen contained an average of 1020 ng of magnetite. Analyses of the single cell magnetic dipole moment of 31 *R. bilocularis* using a miniaturised atomic magnetometer revealed that their magnetic response is based on a permanent magnetic dipole moment (M) per cell, which ranged from 1.10×10^{-14} to 1.51×10^{-11} J/T. The ratio of magnetic to thermal energy, $MB/k_B T$, calculated from the average upper limit

1. Laboratory of Deep-Sea Geology and Geochemistry, Institute of Deep-Sea Science and Engineering, Chinese Academy of Sciences, Sanya, 572000, China
2. University of Chinese Academy of Sciences, Chinese Academy of Sciences, Beijing, 100049, China
3. National Oceanography Centre, European Way, Southampton SO14 3ZH, UK
4. Life Sciences Department, Natural History Museum, Cromwell Road, London SW7 5BD, UK
5. Department of Earth and Atmospheric Sciences, University of Alberta, Edmonton, Alberta T6G 2E3, Canada
6. State Key Laboratory of Lithospheric Evolution, Institute of Geology and Geophysics, Chinese Academy of Sciences, Beijing, China
7. Beijing Synchrotron Radiation Facility, Institute of High Energy Physics, Chinese Academy of Sciences, Beijing, China
8. Jiangsu Key Laboratory of Medical Optics, Suzhou Institute of Biomedical Engineering and Technology, Chinese Academy of Sciences

* Corresponding author (email: xpeng@idsse.ac.cn)



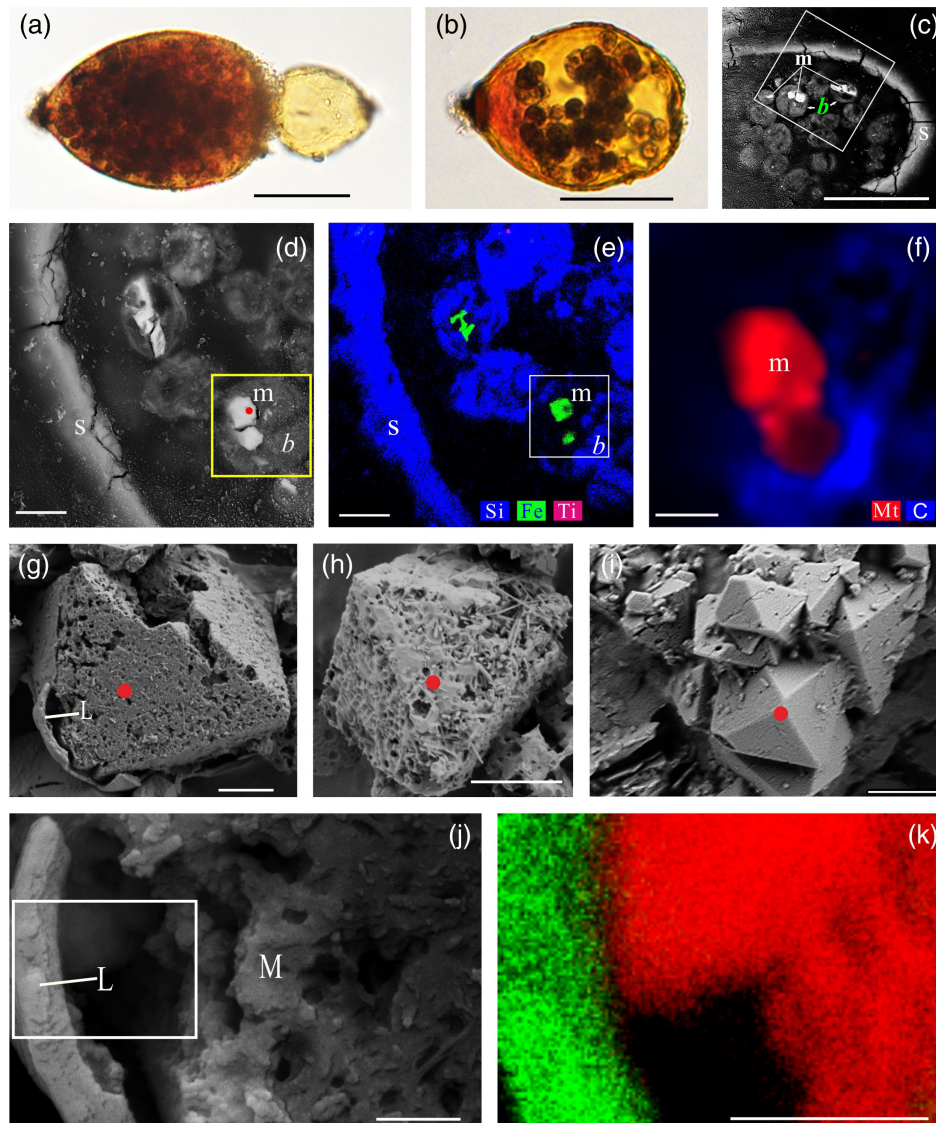


Figure 1 Magnetite in the foraminifera *R. bilocularis*. (a) LM (light microscopy) image showing the rusty colour of the organic walled test of *R. bilocularis* (Gooday *et al.*, 2008). (b) LM image of the larger chamber of *R. bilocularis* stained with Rose Bengal, with fresh stercomata (waste pellets) and stained cytoplasm concentrated just inside the aperture. (c) SEM image of a thin section of *R. bilocularis* from the Challenger Deep with numerous stercomata (*b*) inside the test (*s*). Magnetite (*m*) is contained in the stercomata. (d) Enlarged SEM image of the area indicated by the white rectangle in (c). Magnetite (*m*) is contained in the stercomata (*b*), within the yellow box. Raman analysis position is marked with a red dot. (e) NanoSIMS elemental mapping of *R. bilocularis*. Blue = Si; Green = Fe; Red = Ti. SEM-EDX elemental maps are presented in Figure S-15. (f) Raman spectral combined images obtained from a stercome containing magnetite. Combined maps of intensity of 666 cm^{-1} , 538 cm^{-1} , 304 cm^{-1} (red) and 1367 cm^{-1} , 1582 cm^{-1} (blue), indicating magnetite and organic carbon in stercomata, respectively. (g, h, i) Secondary electron image of magnetite extracted from *R. bilocularis* showing a euhedral and porous structure. L = carbon-containing membrane. (j) An enlarged SEM image of the carbon-containing membrane enveloping the magnetite in Figure 1g. L = carbon-containing membrane, M = magnetite. (k) The elemental mapping of the area in white rectangular of Figure 1j. Green = carbon; Red = iron; other elements are shown in Figure S-16. Scale bars of a,b = 50 μm , c = 20 μm , d,e = 8 μm , f-i = 2 μm , j,k = 0.5 μm .

of M for the foraminifera, is 9.974×10^4 (Table S-2). The magnetic energy of *R. bilocularis* is therefore obviously much greater than the thermal energy.

Characteristics of magnetite in foraminifera. Tests of *Resigella bilocularis* contain numerous stercomata (Fig. 1a,b), waste pellets that are also present in many other hadal monothalamid foraminifera (Gooday *et al.*, 2008). Scanning electron microscopy (SEM), light microscopy and confocal laser scanning microscopy (CLSM) observations revealed multiple particles contained in the stercomata, but absent in the cytoplasm (Fig. 1c,d; Fig. S-1a,b; Fig. S-2; Fig. S-3a,b; Fig. S-4a). They are of variable size (0.15–12 μm) and not arranged in chains (Video S-2, Fig. 2c). These euhedral magnetite particles are octahedral and exhibit a

porous structure (Fig. 1g-i). Secondary ion mass spectrometry (NanoSIMS) and SEM-based energy dispersive X-ray spectroscopy (EDX) revealed that they are mainly composed of Fe and O (Fig. 1e; Fig. S-4c; Fig. S-5b). Raman spectroscopy analyses further showed that they are magnetite particles (Fig. S-4b; Fig. S-6a; Fig. S-7f-h), which are commonly encapsulated by lipid membranes (Fig. 1g,j,k; Fig. 3; Fig. S-3). This is consistent with the results of synchrotron phase contrast analysis experiments showing intact porous magnetite inside stercomata (Fig. 2e; Fig. S-1e-l). The magnetic properties of the foraminifera therefore clearly originate from these micron-sized magnetite particles.

Comparison of magnetite within foraminifera with that from sediments. The magnetite crystals in the stercomata of *R.*

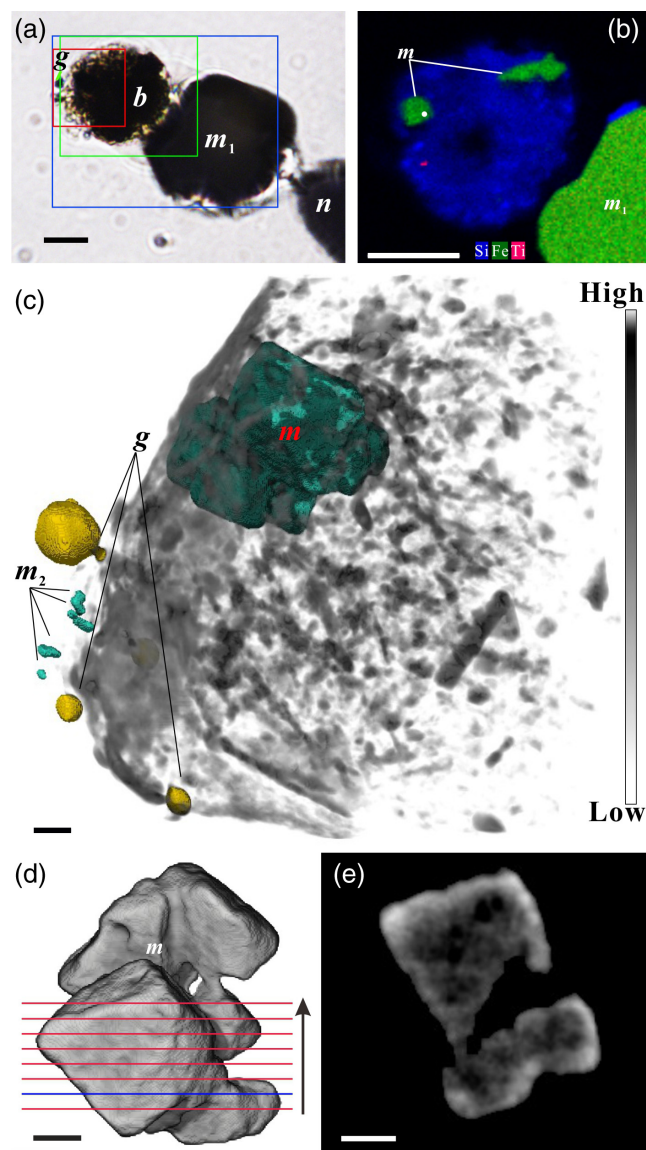


Figure 2 Synchrotron X-ray computerised tomography of a stercome from *R. bilocularis*. (a) Transmitted light micrograph of a stercome. The stercome (b) was placed on the tip of a metal needle (n) adhered to a titanomagnetite standard sample (m_1) and labelled with a gold particle (g). (b) The elemental distribution image characterised by SEM-EDX analysis of stercomata (green box in Fig. 2a). The stercome contains magnetite (m) and rutile (red dot location). (c) A phase contrast image of the foraminiferal stercome (red box range in Fig. 2a) based on synchrotron X-ray computerised tomography (NanoCT) analysis. The absorbance of the foraminiferal magnetite (m) is similar to that of the standard magnetite (m_2), less than that of the gold particle (g). (d) 3D reconstructions of magnetite from synchrotron X-ray computerised tomography. The same particle as that marked 'm' in Figure 2c is shown in eight cross sections from bottom to top in the direction of the arrow in Figure S-1e–l. The 3D reconstructions of the sections indicated by the red and blue lines in Figure 2d have a spatial spacing of 0.296 μm . (e) The 3D reconstruction of the section indicated by the blue line in Figure 2d shows the porous structure of the magnetite. Scale bars of c–e = 1 μm , others = 10 μm .

bilocularis differ in a number of respects from magnetite found in the surrounding hadal sediments. First, they commonly have an octahedral and porous structure (Fig. 1g–i), whereas magnetite in the environmental sediment has an irregular shape, smooth surfaces (Fig. S-8a) and a larger particle size (Fig. S-9; Fig. S-10). Second, magnetite particles within the foraminifera are

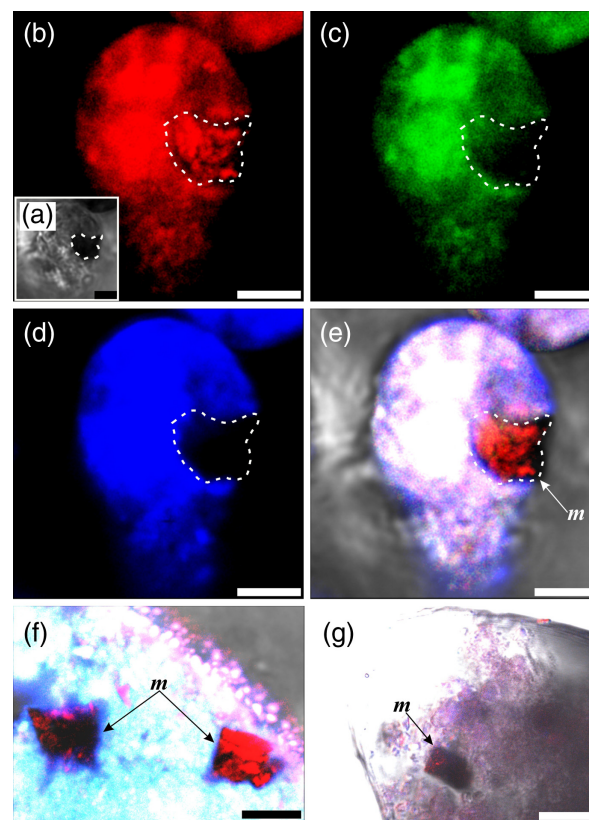


Figure 3 Magnetite (m) encrusted by lipid envelope in a stercome of *R. bilocularis*. (a) Reflected light micrograph of the stercome. (b) CLSM image of the stercome stained using Sudan IV to stain lipid shown in red. (c) CLSM image of the stercome stained using phalloidin to stain actin shown in green. (d) CLSM image of the stercome stained using DAPI to stain DNA shown in blue. (e) Combined image of b–d. A magnetite particle encrusted by a lipid membrane shown in red. (f, g) Combined images showing magnetite encrusted by a lipid membrane stained using Sudan IV. Magnetites are marked with arrow and m. Scale bars of f = 5 μm , g = 10 μm , others = 2.5 μm .

wrapped in an organic envelope, in contrast to those from surrounding sediments, which lack this feature (Fig. 1e–k; Fig. S-3). Third, EDX analyses of magnetite particles from foraminifera demonstrated that they contain no inclusions, whereas silicate-like, magnesium oxide-like, and chrome-aluminum oxide-like inclusions are present in the magnetite from sediments, a feature shared with hydrothermal and magmatic magnetite (Ciobanu *et al.*, 2019) (Fig. S-11; Fig. S-12). Fourth, a magnetic property measurement system (MPMS) yielded a lower transition temperature (104 K) for the foraminiferal magnetite than the magnetite from sediments (111 K) (Fig. S-13).

Discussion

Origin of magnetite in *R. bilocularis*. The porous structure in non-biogenic magnetite generally occurs during the terrestrial weathering of magnetite to hematite (Anand and Gilkes, 1984), or as a result of the formation of magnetite during the reduction of hematite in the solid phase (Deo *et al.*, 1989). The magnetite in *R. bilocularis* did not contain any hematite that would be produced during the weathering of magnetite or left as a residue during the reduction of hematite. Hence, it is not likely that the porous structure associated with magnetite in *R. bilocularis* originates from the weathering (*i.e.* corrosion) of magnetite or the reduction of

hematite. The euhedral structure of magnetite from *R. bilocularis*, which distinctly differs from the irregular shape of magnetite from sediments, also indicates that they might have different origins. The porous structure is possibly formed due to the incorporation of organic matter into the magnetite during the formation process, as indicated by SEM-EDX analyses (Fig. S-5). The formation of minerals with porous structures due to the involvement of organic matter is also a common feature of biologically induced mineralisation (Sanz-Montero *et al.*, 2009).

The differences between the magnetite in *R. bilocularis* stercomata and the magnetite from surrounding sediments further suggests that the former may be produced within the foraminifera, as also reported for certain other protists (Leão *et al.*, 2020). Foraminiferal magnetite is encapsulated by a lipid membrane, which is also more consistent with a biogenic origin. Moreover, the relatively low transition temperature (104 K) of the foraminiferal magnetite is similar to that of biogenic magnetite produced by magnetotactic bacteria (Li *et al.*, 2010; Jackson and Bruce, 2021), perhaps providing additional indirect evidence for biogenic origin.

High throughput sequencing of *R. bilocularis* failed to reveal the presence of any associated magnetotactic bacteria, although about 0.09 % of sequences were attached to the iron reducing bacterium *Shewanella* sp. (Fig. S-14). The sequences had 94.47 % similarity with *Shewanella piezotolerans* WP3 which was isolated from deep sea sediments (Wang *et al.*, 2004). The magnetite synthesised by *S. piezotolerans* WP3 is commonly 4–8 nm in diameter and significantly smaller than that found in *R. bilocularis* (Wu *et al.*, 2013). Thus, a purely bacterial origin for the magnetite particles found in *R. bilocularis* is unlikely.

Biologically controlled mineralisation typically generates magnetite crystals with a uniform morphology, high chemical purity and arranged in chains, whereas biologically induced mineralisation (BIM) generates magnetite crystals of variable size and morphology that are not arranged in chains (Bazylinski *et al.*, 2007). The presence of a lipid membrane, together with the morphological and chemical characteristics of the *R. bilocularis* crystals, favours the hypothesis that they are most likely formed through BIM in microenvironments within stercomata. However, the collection of mineral grains is typical of foraminifera and therefore we cannot completely rule out the possibility that magnetite may be derived from surrounding sediments.

The iron reducing bacterium *Shewanella* sp. detected in *R. bilocularis* may be involved in magnetite biomineralisation within *R. bilocularis* via providing a Fe^{2+} source. We develop

the following conceptual model for the formation of magnetite in foraminifera (Fig. 4). The foraminifera first feed on the iron oxides that are commonly present in the surface sediments. The semi-enclosed environment within the foraminiferal test provides conditions that permit *Shewanella* sp. to reduce Fe^{3+} in iron oxides to Fe^{2+} . Generated Fe^{2+} within the foraminiferal test then is transported into the stercomata where micron-sized magnetite is formed in the presence of organic matter (Fig. S-5a).

Implications

Regardless of whether magnetite in *R. bilocularis* has a biological origin or is derived from surrounding sediments, their passive response to the magnetic field make them the first example of magnetic protist at hadal depths. In magnetotactic bacteria and algae, the magnetic energy is sufficient to overcome the irregular motion induced by external thermal energy, allowing these microorganisms to exhibit magnetotactic behaviour (Araujo *et al.*, 1986; Pan *et al.*, 2005). Although the magnetic energy in *R. bilocularis* is also larger than external thermal energy, this does not mean that these foraminifera must have magnetotactic capability, because larger particles, such as foraminifera 100–200 μm in size are less affected by the Brownian motion than much smaller microbial organisms (Russel, 1981). Whether the magnetite in *R. bilocularis* fulfills any physiological function remains unknown. Perhaps, these foraminifera may take advantage of the magnetite to sense the Earth's magnetic field, like some ciliates and flagellates (Monteil and Lefevre, 2020) or adjust the iron balance within the test (Andrews *et al.*, 2003). *In situ* experiments are needed to test these possibilities and better understand the origin of the magnetite crystals and other aspects of the biology of these very common but enigmatic hadal protists.

Acknowledgements

We are grateful to the crew of R/V TANSUOYIHAO for their hard work during the expedition (TS01 to TS14). We also appreciate the help and advice provided by Xue Liang and Yifeng Li of Shanghai University in the FIB-TEM analysis; Ye Li of the Institute of Environment and Plant Protection, Chinese Academy of Tropical Agricultural Sciences (Haikou) for her help during the production of ultrathin sections; and Jialong Hao of the Institute of Geology and Geophysics, Chinese Academy of Sciences for his help in the NanoSIMS tests. We thank Zixiao Guo of Hebei Normal University for providing detailed methods on sample preparation. We would like to thank Dong Sheng, Qianqian Yu and Siqi Liu of the University of Science and Technology of China for their guidance and assistance during the atomic magnetometer analysis. We also express our gratitude to Qingxi Yuan, Jin Zhang, Kai Zhang, Tianyu Fu and Chunxia Yao at the Beijing Synchrotron Radiation Facility (BSRF) for their help with hard X-ray phase contrast imaging and computed tomography (CT) analysis. We thank Hanna Han and her team from Shenzhen Ecogene Co., Ltd. for their technical service. We thank Zhuoli Zhao of China University of Geosciences (Beijing) for the data processing of 16S high-throughput sequencing. This study was financially supported by the National Key Research and Development Program of China (Grant No. 2016YFC0304900). We thank two anonymous reviewers for their comments which led to substantial improvements in the manuscript.

Editor: Juan Liu

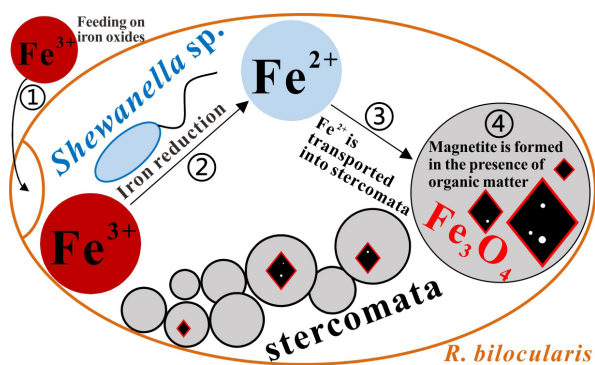


Figure 4 A conceptual model of formation of magnetite in *R. bilocularis*. 1) Foraminifera feed on sediments containing iron oxides (Fe^{3+}). 2) Reduction of Fe^{3+} to Fe^{2+} by the iron reducing bacterium *Shewanella* sp. 3) Fe^{2+} is transferred to the stercomata. 4) Formation of porous magnetite with organic matter incorporated. The red rhombs represent lipid envelopes.

Additional Information

Supplementary Information accompanies this letter at <http://doi.org/10.7185/geochemlet.2212>.



© 2022 The Authors. This work is distributed under the Creative Commons Attribution Non-Commercial No-Derivatives 4.0

License, which permits unrestricted distribution provided the original author and source are credited. The material may not be adapted (remixed, transformed or built upon) or used for commercial purposes without written permission from the author. Additional information is available at <https://www.geochemicalperspectivesletters.org/copyright-and-permissions>.

Cite this letter as: Yang, H., Peng, X., Gooday, A.J., Jones, B., Li, J., Liu, S., Huang, W., Sun, Z., Chen, S., Dasgupta, S., Xu, H., Liu, S., Xu, W., Ta, K. (2022) Magnetic foraminifera thrive in the Mariana Trench. *Geochem. Persp. Let.* 21, 23–27. <https://doi.org/10.7185/geochemlet.2212>

References

- ANAND, R.R., GILKES, R.J. (1984) Mineralogical and chemical properties of weathered magnetite grains from lateritic saprolite. *European Journal of Soil Science* 35, 559–567. <https://doi.org/10.1111/j.1365-2389.1984.tb00613.x>
- ANDREWS, S.C., ROBINSON, A.K., RODRÍGUEZ-QUIÑONES, F. (2003) Bacterial iron homeostasis. *FEMS Microbiology Reviews* 27, 215–237. [https://doi.org/10.1016/S0168-6445\(03\)00055-X](https://doi.org/10.1016/S0168-6445(03)00055-X)
- ARAUJO, F.D., PIRES, M.A., FRANKEL, R.B., BICUDO, C. (1986) Magnetite and magnetotaxis in algae. *Biophysical Journal* 50, 375–378. [https://doi.org/10.1016/S0006-3495\(86\)83471-3](https://doi.org/10.1016/S0006-3495(86)83471-3)
- BAZYLINSKI, D.A., FRANKEL, R.B. (2004) Magnetosome formation in prokaryotes. *Nature Reviews Microbiology* 2, 217–230. <https://doi.org/10.1038/nrmicro842>
- BAZYLINSKI, D.A., FRANKEL, R.B., KONHAUSER, K.O. (2007) Modes of biomineralization of magnetite by microbes. *Geomicrobiology Journal* 24, 465–475. <https://doi.org/10.1080/01490450701572259>
- BAZYLINSKI, D.A., LEFÈVRE, C.T., FRANKEL, R.B. (2012) Magnetotactic protists at the oxic–anoxic transition zones of coastal aquatic environments. *Anoxia* 21, 131–143. https://doi.org/10.1007/978-94-007-1896-8_7
- CIOBANU, C.L., VERDUGO-IHL, M.R., SLATTERY, A., COOK, N.J., EHRIG, K., COURTNEY-DAVIES, L., WADE, B.P. (2019) Silician magnetite: Si–Fe–nanoprecipitates and other mineral inclusions in magnetite from the Olympic Dam Deposit, South Australia. *Minerals* 9, 311–346. <https://doi.org/10.3390/min9050311>
- DEO, B., DUBE, R.K., CHATTERJI, S. (1989) Formation of porous magnetite in the initial stages of solid state reduction of hematite by metallic iron. *ISIJ International* 29, 345–347. <https://doi.org/10.2355/isijinternational.29.345>
- FRANKEL, R.B. (1984) Magnetic Guidance of Organisms. *Annual Review of Biophysics and Bioengineering* 13, 85–103. <https://doi.org/10.1146/annurev.bb.13.060184.000505>
- GOODAY, A.J., TODO, Y., UEMATSU, K., KITAZATO, H. (2008) New organic-walled Foraminifera (Protista) from the ocean’s deepest point, the Challenger Deep (western Pacific Ocean). *Zoological Journal of the Linnean Society* 3, 399–423. <https://doi.org/10.1111/j.1096-3642.2008.00393.x>
- JACKSON, M.J., BRUCE, M. (2021) On the distribution of Verwey transition temperatures in natural magnetites. *Geophysical Journal International* 2, 1314–1325. <https://doi.org/10.1093/gji/ggaa516>
- KIRSCHVINK, J.L., WALKER, M.M., DIEBEL, C.E. (2001) Magnetite-based magnetoreception. *Current Opinion in Neurobiology* 11, 462–467. [https://doi.org/10.1016/S0959-4388\(00\)00235-X](https://doi.org/10.1016/S0959-4388(00)00235-X)
- LI, J.H., PAN, Y.X., LIU, Q.S., QIN, H.F., DENG, C.L., CHE, R.C., YANG, X.A. (2010) A comparative study of magnetic properties between whole cells and isolated magnetosomes of magnetospirillum magneticum AMB-1. *Chinese Science Bulletin* 55, 38–44. <https://doi.org/10.1007/s11434-009-0333-x>
- LEÃO, P., LE NAGARD, L., YUAN, H., CYPRIANO, J., DA SILVA-NETO, I., BAZYLINSKI, D.A., ACOSTA-AVALOS, D., BARROS, H.L., HITCHCOCK, A.P., LINS, U., ABREU, F. (2020) Magnetosome magnetite biomineralization in a flagellated protist: evidence for an early evolutionary origin for magnetoreception in eukaryotes. *Environmental Microbiology* 22, 1495–1506. <https://doi.org/10.1111/1462-2920.14711>
- MANN, S., FRANKEL, R.B., BLAKEMORE, R.P. (1984) Structure, morphology and crystal growth of bacterial magnetite. *Nature* 310, 405–407. <https://doi.org/10.1038/310405a0>
- MAUGH, T. (1982) Magnetic navigation an attractive possibility. *Science* 215, 1492–1493. <https://doi.org/10.1126/science.7063857>
- MONTEIL, C.L., LEFÈVRE, C.T. (2020) Magnetoreception in Microorganisms. *Trends in Microbiology* 28, 266–275. <https://doi.org/10.1016/j.tim.2019.10.012>
- PAN, Y., PETERSEN, N., DAVILA, A.F., ZHANG, L.M., WINKLHOFFER, M., LIU, Q.S., HANZLIK, M., ZHU, R.X. (2005) The detection of bacterial magnetite in recent sediments of Lake Chiemsee (southern Germany). *Earth and Planetary Science Letters* 232, 109–123. <https://doi.org/10.1016/j.epsl.2005.01.006>
- RUSSEL, W.B. (1981) Brownian motion of small particles suspended in liquids. *Annual Review of Fluid Mechanics* 13, 425–455. <https://doi.org/10.1146/annurev.fl.13.010181.002233>
- SANZ-MONTERO, M.E., RODRÍGUEZ-ARANDA, J.P., CURA, M. (2009) Bioinduced precipitation of barite and celestite in dolomite microbialites: Examples from Miocene lacustrine sequences in the Madrid and Duero Basins, Spain. *Sedimentary Geology* 222, 138–148. <https://doi.org/10.1016/j.sedgeo.2009.05.009>
- SCHOENLE, A., HOHLFELD, M., HERMANN, K., MAHE, F., VARGAS, C.D., NITSCH, F., ARNDT, H. (2021) High and specific diversity of protists in the deep-sea basins dominated by diplomonads, kinetoplastids, ciliates and foraminiferans. *Communications Biology* 4, 501–511. <https://doi.org/10.1038/s42003-021-02012-5>
- TODO, Y., KITAZATO, H., HASHIMOTO, J., GOODAY, A.J. (2005) Simple foraminifera flourish at the ocean’s deepest point. *Science* 307, 689–689. <https://doi.org/10.1126/science.1105407>
- UEBE, R., SCHÜLER, D. (2016) Magnetosome biogenesis in magnetotactic bacteria. *Nature Reviews Microbiology* 14, 621–637. <https://doi.org/10.1038/nrmicro.2016.99>
- WANG, F.P., WANG, P., CHEN, M.X., XIAO, X. (2004) Isolation of extremophiles with the detection and retrieval of Shewanella strains in deep-sea sediments from the west Pacific. *Extremophiles* 8, 165–168. <https://doi.org/10.1007/s00792-003-0365-0>
- WU, W.F., WANG, F.P., LI, J.H., YANG, X.M., PAN, Y.X. (2013) Iron reduction and mineralization of deep-sea iron reducing bacterium Shewanella piezotolerans WP3 at elevated hydrostatic pressures. *Geobiology* 11, 593–601. <https://doi.org/10.1111/gbi.12061>



Magnetic foraminifera thrive in the Mariana Trench

H. Yang, X. Peng, A.J. Gooday, B. Jones, J. Li, S. Liu, W. Huang, Z. Sun, S. Chen, S. Dasgupta, H. Xu, S. Liu, W. Xu, K. Ta

Supplementary Information

The Supplementary Information includes:

- Material and Methods
- Tables S-1 to S-3
- Figures S-1 to S-16
- Videos S-1 and S-2
- Supplementary Information References

Material and Methods

Samples

Specimens of the foraminiferal species *R. bilocularis* used for mineralogy, isotope geochemistry and magnetic study were obtained from box core No. TS01-B10 at 11°11.7' N, 141°48.7'E (8638 m water depth) and stored at 4 °C, –20 °C, and –80 °C respectively. Specimens for morphological study and staining were recovered from the Challenger Deep (11°16.4'N, 142°18.8'E; water depth 9946 m; box core No. TS14-B01), stored at –80 °C for 7 months and stained with Rose Bengal (1.0 g L⁻¹) overnight at room temperature (see Fig. 1b). Other material collected from TS14-B01 was preserved in 4 % paraformaldehyde at 4 °C and stained with Rose Bengal (0.5 g L⁻¹) after one month (See Fig. 1a). The upper 5 cm layer of sediment was examined in this study.

Hadal foraminifera were mainly found at the bottom of the trench and on flat ground in front of relatively gentle slopes. At our main study site (TS01-B10) the number of *R. bilocularis* specimens (dead and living) *per* gram of wet sediment was 10–15. Based on 55 individuals, *R. bilocularis* were typically 190–220 µm in length, 45–60 µm (smaller chamber) and 70–85 µm (larger chamber) in width.

Pre-processing of samples

Rose Bengal dyeing experiments

The sediment was sieved with deionised water on a 63-µm-mesh copper sieve at room temperature. The sieve containing the residue was then placed in a bowl of stain (1 g of Rose Bengal in 1 L of ultrapure water) and left overnight at room temperature. After staining, the residue from the sieve was transferred to a Petri

dish and the foraminifera were picked out with a pipette. Finally, the foraminifera were placed in glycerol on a cavity slide, covered with a coverslip and observed under a light microscope. Specimens of *R. bilocularis* stained a reddish colour with the protoplasmic dye Rose Bengal (Fig. 1a,b) (Murray and Bowser, 2000; but see Bernhard *et al.*, 2006).

Magnetite enrichment and preparation

Magnetite enrichment in foraminifera was studied in the Laboratory of Deep-Sea Geology and Geochemistry at IDSSE, building on the procedure described by Matthieu Amor (Amor *et al.*, 2015). Magnetite samples from foraminifera used for low temperature magnetic tests and iron isotope experiments were prepared as follows. More than 1000 foraminifera were picked manually from surface sediments from TS01-B10 after sieving on a 63- μm screen. The main changes compared to the method of Amor *et al.* (2015) were the choice of a different mechanical crushing method and the use of heavy liquid sodium polytungstate. The test and its contents were digested in TES buffer and phenol solution, then crushed in a ball mill for 1.5 min without the use of silica balls (MiniBeadbeater-16, repeated 5 times with 20 s gaps to dissipate heat and eliminate air bubbles). TES buffer was prepared by mixing SDS (1 wt. %), Triton X-100 (0.5 wt. %), EDTA (10 mM, from an EDTA solution stored at pH 8.0), Tris buffer (10 mM, from a Tris solution stored at pH 7.4), and ultrapure water. After extraction from the foraminifera, the mixture containing magnetite was reacted with a solution consisting of TES buffer (0.6 mL) and phenol (0.6 mL) at 70 °C for 12 hours. Magnetite was collected with a magnet and pipette gun after being centrifuged for 45 minutes (4500 r/min) with sodium polytungstate (3 g/cm³). Between each step, the sample was ultrasonicated (100 Hz) for 5 minutes. Before each reagent change, the sample was centrifuged with ultrapure water repeatedly at high speed (12,000 r/min for 10 min) to remove the overlying liquid phase and dried in an oven at 60 °C. Finally, the enriched magnetite was washed five times with ultrapure water and transferred to wax paper for magnetic and isotopic analysis.

The samples (Fig. 1g–i) used for the morphological analysis of magnetite from foraminifera were prepared as follows. Foraminifera were handpicked from the surface sediment of the B10 box samples using a stereo microscope, rinsed with ultrapure water, and placed in a centrifuge tube. Ultrapure water was added to fill half the volume of the centrifuge tube and processed for 1.5 minutes using a Mini Beadbeater-16 bead-mill type grinder (without added silica balls) and this process repeated 3 times. This was followed by sonication with an ultrasonicator for 5 minutes and centrifugation for 1.5 minutes using a high-speed centrifuge (12,000 rpm), repeated six times. The aqueous solution of the sample was then placed in a Petri dish and the magnet and pipette were used to sort out the magnetite aggregates (magnets were not in direct contact with the sample).

Magnetite from the environment was collected from sediments from which all foraminifera that had been removed by magnetic separation followed by manual selection.

Micro analysis

Light microscopy (LM)

Optical microscope photography was also conducted in the Laboratory of Deep-Sea Geology and Geochemistry at IDSSE. The foraminifera in Figure 1a,b were photographed with a Leica DM6000 microscope using transmission mode (bright field). Resin polished thin sections of individual foraminiferal stercomata in Figures 2a and S-4a were analysed using a Leica DM2700P polarising light microscope in transmission and reflection mode, respectively.

Confocal laser scanning microscopy (CLSM) analysis

Staining of foraminiferal cells was carried out at the SUZHOU Institute of Biomedical Engineering and Technology, Chinese Academy of Sciences, using a Leica confocal laser scanning microscopy (Leica SP5, with 60 \times objective). The distributions of the magnetite and the cell body were analysed by staining



foraminifera with diamidinophenolindole (DAPI), Sudan IV, and phalloidin according to the following procedure. After thawing the sediment samples stored at $-20\text{ }^{\circ}\text{C}$, foraminifera were collected, fixed in 4 % paraformaldehyde, and kept at $4\text{ }^{\circ}\text{C}$. The fixative was washed off with ultrapure water and the foraminifera were transferred to a glass bottom dish (0.13–0.16 mm, Cellvis) using a pipette gun. Then, two drops of phalloidin (10 $\mu\text{g}/\text{mL}$ stock solution; excitation/emission wavelength, 488/497–539 nm), two drops of DAPI (10 $\mu\text{g}/\text{mL}$ stock solution; excitation/emission wavelength, 405/417–481 nm) and four drops of Sudan IV (add 0.1 g Sudan IV to 50 mL acetone, and dilute to a final volume of 100 mL with 75 % alcohol; excitation/emission, 488 and 514/565–623 nm) were added in that order using a 20 μL pipette gun and kept at $4\text{ }^{\circ}\text{C}$ with a sealing membrane overnight. Finally, the samples were washed five times with ultrapure water and transferred to another confocal Petri dish with a glycerol droplet for observation under Leica confocal microscope.

Scanning electron microscopy (SEM) and elemental mapping

Scanning electron microscopy and energy dispersive X-ray spectroscopy (EDX) were performed at IDSSE using a ThermoScientific Apreo C instrument. Specimens were mounted on an aluminum stub with carbon tape and the surfaces were sputtered with Au. The SEM was operated at 2 kV with a working distance of ~ 10 mm and images were taken in backscattered electron (BSE) imaging mode. An accelerating voltage of 10 kV was used in the X-ray elemental mapping analysis to obtain sufficient X-ray counts.

Hard X-ray phase contrast imaging and computed tomography (CT) analysis

Hard X-ray phase contrast imaging and computed tomography (CT) of stercomata was performed at the Beijing Synchrotron Radiation Facility (BSRF), Institute of High Energy Physics (IHEP) of the Chinese Academy of Sciences, using a 4W1A beamline. The instrument has a spatial resolution of 50 nm. Sample preparation and testing procedures were as follows. One environmental magnetite and one foraminifera stercome were attached in turn to the tips of Huatuo brand acupuncture needles (0.25×50 mm) with Super-Fast Epoxy-Cement AB. Spherical granular gold (Alfa Aesar, 1.5–3.0 μm , Lot # F21S031) and a 99.99 % granular magnetite standard sample were dipped with PE fibers and adhered to the upper surface of the stercomata as markers. Ten background analyses were obtained prior to sample analysis. Photon counts were greater than 4000. Single sheet analysis time was 17 seconds. 361 projection images were shot by rotating the stercome from -90° to $+90^{\circ}$ angle at 0.5° intervals. The data were processed by background subtraction, image geometry correction and axis correction. During reconstruction, Binning = 1, RingRemoved was selected for low contrast, the output data type was 16 bit, and Recon Filters were smoothed (kernel size = 1.2). The data were acquired using the software ZEISS XM Controller. The software TXMcontroller was used to deduct background and image geometry correction. TXMReconstructor was used for axis correction and reconstruction of tomography images. TXM3DViewer was used for 3D reconstruction.

Mineral identification

Raman spectroscopy

Raman spectroscopy experiments were done at IDSSE. We used a WiTec alpha300 R (WiTec GmbH) confocal Raman imaging system with a 532 nm Nd:YAG laser beam, a 600 or 1200 grooves/mm grating and a $100\times$ objective (NA = 0.75) providing a horizontal resolution of 0.35 μm . The laser power on the sample surface was maintained between 0.1 and 0.5 mW during the test with an integration time of ~ 15 seconds.

Dual beam focused ion beam (FIB) and Transmission electron microscopy (TEM)

To prepare TEM sections from magnetite crystals fixed to a carbon film, FIB milling was performed with FEI Helios 600i FIB at the Analysis and Research Center, Shanghai University, China. A layer of platinum was deposited over a region of interest to protect the surface from ion-beam damage during the milling processes. The thin sections were lifted out and fixed to a copper grid for energy dispersive X-ray (EDX)-Mapping analysis, which were carried out at 200 Kv in a TEM JEM-2100F field emission microscope.



Ultra-thin section of *R. bilocularis* in Figure S-2 was made by Laica UC6 and TEM image was obtained using a JEM-2100F field emission microscope operating at 120 kV at the Institute of Zoology and Botany, Chinese Academy of Tropical Agricultural Sciences (Haikou).

Geochemical analysis

NanoSIMS ion mapping

NanoSIMS elemental mapping was carried out on foraminiferal resin thin sections using a Cameca NanoSIMS 50L (Cameca, Paris, France), at the Institute of Geology and Geophysics, Chinese Academy of Sciences. To remove the conductive coating (Au) and contaminants generated during pretreatment, the analysed area was pre-sputtered with a beam current of 150 pA and an ion dose of $N = 5 \times 10^{16}$ ions/cm². In multi-collection mode, negative secondary ions (¹²C⁻, ²⁸Si⁻, ⁴⁸Ti¹⁶O⁻, ⁴⁰Ca¹⁶O⁻, ³²S⁻, and ⁵⁶Fe¹⁶O⁻) were sputtered from the sample surface using a Cs⁺ primary beam with an intensity of ~2.5 pA. Figure 1e is 256 × 256 pixels and was recorded over a period of ~30 min.

Isotope geochemistry

Four enriched magnetite samples were used for Fe isotope analysis: samples No. 1 and No. 2 were magnetite collected from environmental sediments from which foraminifera had been completely removed, and samples No. 3 and No. 4 were magnetite concentrated from approximately 500 specimens of *R. bilocularis*. The method used to enrich magnetite from foraminifera was refined from Matthieu Amor (Amor *et al.*, 2015), as described above.

Measurements of Fe isotope ratios were performed using MC-ICP-MS (NEPTUNE PLUS, Thermo Scientific) at the Swedish solid isotope laboratory (ALS) using internal standardisation for δ^{56} and $\delta^{57/54}$. The entire contents of the sample container were transferred to a Teflon tube and digested using a mixture of AR+HF [0.7 mL hydrochloric acid (12.1 mol/L), 0.3 mL HNO₃ (15.9 mol/L) and 0.02 mL HF (29.9 mol/L)]. The digest was evaporated to dryness, the residue was absorbed in 0.2 mL hydrochloric acid, and the iron was separated by ion exchange. All analyses were carried out in the order of the isotope standards. Delta values for Fe were calculated against IRMM-014 CRM using SRMs as an external calibration. SD was calculated from two independent consecutive measurements (Malinovsky *et al.*, 2003). All samples were taken in duplicate, except for samples No. 3 and No. 4, which contained a limited amount of foraminiferal magnetite.

Magnetic studies

Magnetic studies

We apply the term ‘magnetic’ in a strict sense to those organisms containing biogenic magnetite and passively orientating in response to an applied magnetic field. ‘Magnetotactic’ organisms have the additional capability to move actively under the influence of an applied magnetic field (Lins and Bazylinski, 2009).

Specimens of *R. bilocularis* were collected from sediments and transferred to a plastic Petri dish containing ultrapure water. On the ship immediately after collection of the samples (TS14-B01), those stained by Rose Bengal (Fig. 1a,b) were found to orientate passively in response to an applied magnetic field (Video S-1). Most of the specimens used for magnetic study were collected with box cores (TS01-B10) at 11°11.7' N, 141°48.7'E (8638 m water depth), stored at 4 °C, and picked from sediments in the land-based laboratory later for low-temperature magnetic tests (Fig. S-13) and subsequent isotope geochemical analysis (Table S-3). Their magnetic responses were observed microscopically in drops of ultrapure water with a small bar magnet or Helmholtz coils (5.0–200 GS, 3.4Ω) placed on the microscope stage, as previously described by Blakemore and Frankel (1981), both on the ship and in the land-based IDSSE laboratory. In both cases, the video of this experiment was shot using a Leica M205C stereoscope; only the video shot at



IDSSE is shown in the supporting information (Video S-1), as wind and waves affected the clarity of the shots on the ship.

The low temperature magnetic tests on magnetite were conducted with a magnetic measurement system (MPMS XP-5) at the Laboratory of Rock Magnetism and Paleomagnetism, Institute of Geology and Geophysics, Chinese Academy of Sciences. Samples were cooled from 300 K to 5 K in a zero magnetic field, pulsed with a saturating magnetic field of 5 T (SIRM_{5 T-5 K}), and then heated from 5 K to 300 K in a zero magnetic field to measure remanence magnetisations (ZFC). Afterwards, the sample was cooled from 300 K to 5 K in a 5 T magnetic field and then heated from 5 K to 300 K in a zero magnetic field to measure the remanence magnetisation (FC). During isothermal remanence magnetisation (IRM) acquisition and measurement, the sample was held at 5 K. IRM was generated by pulsing the sample with an axial field from 0 T to 5 T. Empty *Resigella* tests were tested under the same conditions to deduct the effect of the background signal on the results. The detection limit of MPMS was 1E-9 emu and the sensitivity was $\pm 5.0 \times 10^{-10}$ Am².

Miniaturised atomic magnetometer

Foraminiferal single-cell magnetic dipole moments were measured at the Department of Precision Machinery and Precision Instruments of the University of Science and Technology of China, using a miniaturised atomic magnetometer developed independently by the Department. The sensitivity of the miniaturised atomic magnetometer was 40 fT/ $\sqrt{\text{Hz}}$ in a noisy environment at a frequency of 50 Hz. Adhesive tape with foraminifera was fixed to the front of the sample carrying rod, and the sample-to-probe magnetic remanence was measured at 1 mm intervals, with 10 groups (7–16 mm) for each sample. The remanence of foraminifera placed perpendicular to the z-direction of the modulation field of the atomic magnetometer was measured at angular distances 45° apart. The test was repeated once, and the arithmetic mean of the test results was taken to eliminate data fluctuations caused by changes in the instrument over time. The average magnetic dipole moment of the sample carrying rod with high temperature tape was measured as a background value and deducted. The magnetic dipole moment of each foraminifer was obtained by fitting 10 sets of data according to the formula for the magnetic field distribution of the magnetic dipoles. The fitting formula is $B = \mu_0/4\pi * M/x^3 + c$, where B is the magnetic field strength, M is the magnetic dipole moment, μ_0 is the vacuum permeability and c is the deviation. The magnetic dipole moments of the empty sample rods and tapes, as well as the magnetic dipole moments of the rods and tapes with attached foraminiferal specimens, were measured five times to calibrate the standard deviation of the test data due to operational errors.

*High-throughput sequencing of the 16S rRNA gene of bacteria associated with *R. bilocularis**

Sample preparation. Two sediment samples from TS01-B10, stored separately at 4 °C and -20 °C, were first washed with ultrapure water several times before specimens of *R. bilocularis* were picked (each sample contained 10 specimens), followed by rewashing five times using ultrapure water. The control samples for each of the two collections of samples were the sediments after removal of all foraminifera. The prepared samples were stored at -20 °C until genetic analysis.

DNA Extraction, PCR Amplification, and Illumina MiSeq Sequencing. Microbial DNA was extracted from the samples using the QIAGEN DNeasy PowerSoil kit (Qiagen) according to the manufacturer's protocols. The bacterial 16S rRNA gene was amplified by PCR (94 °C for 3 min, followed by 29 cycles at 95 °C for 30 s, 50 °C for 1 min, and 72 °C for 1 min and a final extension at 72 °C for 10 min) using primers 515F (5'-barcode-GTGCCAGCMGCCGCGGTAA-3') and 806R (5'-GGACTACVSGGGTATCTAAT-3'); the barcode was an eight-base sequence unique to each sample. PCR reactions and the extraction and purification of amplicons were performed according to the report by Gao Pin (Gao *et al.*, 2019). Purified PCR products were quantified using Qubit®3.0 (Life Invitrogen). The pooled DNA product was used to construct Illumina Pair-End library following Illumina's genomic DNA library preparation procedure. Then the amplicon library was paired-end sequenced (2 × 250) on an Illumina MiSeq platform at Ecogene Biotech



(Shenzhen, China) according to the standard protocols. The operational taxonomic units (OTUs) were defined based on 97 % sequence similarity using USEARCH. Each sequence with the highest abundance was selected as representative OTU and was taxonomically assigned against the SILVA123 Database using classifier–sklearn.

The data used in the phylogenetic analysis were based on the OTUs after taxonomic annotation, ignoring the OTUs that were not annotated to families, genera and species, and the data used accounted for 92.97 % of the original OTUs abundance. The sequences with the highest abundance were selected as OTU representative sequences for phylogenetic tree. Multiple alignments were performed by using the CLUSTAL_X software package. Evolutionary distances were calculated with the Kimura two-parameter model. Phylogenetic tree was constructed by using neighbour-joining method with MEGA software version X.

The bacterial 16S rRNA gene sequencing data are publicly available in the NCBI Short Read Archive (SRA) under Bioproject accession No.: PRJNA784647.



Supplementary Tables

Table S-1 Data for stations in the South Mariana Trench at which samples were collected during cruises of the Research Vessel Tansuoyihao (2016–2019).

| Cruise | Deployment | Latitude N | Longitude E | Depth (m) |
|--------|------------|------------|-------------|-----------|
| TS01 | B02 | 10°59.380' | 141°57.870' | 6980 |
| | B10 | 11°11.699' | 141°48.701' | 8638 |
| | LR10 | 11°19.653' | 142°12.114' | 10,822 |
| TS03 | GT01 | 11°11.699' | 141°48.701' | 8638 |
| | LR14 | 11°19.500' | 142°11.316' | 10,911 |
| | TY063 | 11°19.501' | 142°10.743' | 10,894 |
| TS09 | YW019 | 11°20.131' | 142°12.409' | 10,884 |
| | YW020 | 11°20.074' | 142°12.932' | 10,898 |
| | TY038 | 11°19.864' | 142°12.189' | 10,893 |
| TS14 | B02 | 11°14.844' | 142°13.714' | 10,063 |
| | B01 | 11°16.351' | 142°18.796' | 9946 |



Table S-2 Measurements of magnetic dipole moment in *R. bilocularis* using miniaturised atomic magnetometer.

| Sample No. | Magnetic dipole moment (J/T) | Size of foraminifer (μm) | | | Decidability factor | Standard deviation due to operational error |
|------------|------------------------------|---------------------------------------|-------------------------|--------------------------|---------------------|---|
| | | Length | Width of bigger chamber | Width of smaller chamber | | |
| 1 | 1.512E-12 | 230 | 90 | 55 | 0.1767 | 5.88364E-13 |
| 2 | 8.356E-12 | 181 | 80 | 40 | 0.9237 | |
| 3 | 2.69E-12 | 197 | 84 | 48 | 0.9478 | |
| 4 | 5.458E-12 | 206 | 80 | 56 | 0.9076 | |
| 5 | 1.508E-11 | 209 | 81 | 48 | 0.9958 | |
| 6 | 4.454E-13 | 221 | 86 | 58 | 0.0443 | |
| 7 | 3.936E-13 | 131 | 48 | 26 | 0.0244 | |
| 8 | 2.534E-13 | 205 | 76 | 46 | 0.0388 | |
| 9 | 1.095E-14 | 136 | 48 | 31 | 0.0002 | |
| 10 | 4.474E-12 | 217 | 86 | 55 | 0.6173 | |
| 11 | 1.943E-12 | 181 | 75 | 45 | 0.6447 | |
| 12 | 6.831E-12 | 195 | 82 | 44 | 0.9756 | |
| 13 | 1.271E-12 | 169 | 79 | 45 | 0.5906 | |
| 14 | 8.457E-12 | 190 | 75 | 46 | 0.9307 | |
| 15 | 3.885E-12 | 208 | 73 | 45 | 0.8601 | |
| 16 | 9.835E-12 | | | | 0.9887 | |
| 17 | 4.274E-12 | 202 | 81 | 56 | 0.9092 | |
| 18 | 8.755E-13 | 181 | 82 | 40 | 0.4686 | |
| 19 | 1.413E-11 | 143 | 94 | 48 | 0.9919 | |
| 20 | 8.746E-13 | 204 | 82 | 52 | 0.2984 | |
| 21 | 2.854E-13 | 172 | 83 | 36 | 0.3403 | |
| 22 | 1.162E-12 | 214 | 80 | 59 | 0.5707 | |
| 23 | 5.983E-13 | 182 | 78 | 47 | 0.2040 | |
| 24 | 5.788E-13 | | | | 0.6319 | |
| 25 | 2.433E-12 | 211 | 85 | 48 | 0.6907 | |
| 26 | 1.143E-12 | 225 | 83 | 59 | 0.3510 | |
| 27 | 1.113E-12 | 131 | 75 | 39 | 0.4358 | |
| 28 | 5.578E-12 | 191 | 83 | 46 | 0.8270 | |
| 29 | 6.111E-12 | 214 | 83 | 61 | 0.9721 | |
| 30 | 8.501E-12 | 186 | 84 | 60 | 0.9720 | |
| 31 | 6.349E-13 | 189 | 80 | 51 | 0.4456 | |

Note: The standard deviation of these data due to operational error was 5.88364×10^{-13} J/T, indicating low confidence in the lower limit of the M value measured on the test. The average upper limit of M for *R. bilocularis* was 7.63×10^{-12} J/T, based on 13 highly reliable measurements greater than or equal to 10^{-12} J/T, with a coefficient of determination higher than 0.80. The ratio of magnetic to thermal energy, $MB/k_B T$, calculated from the average upper limit of M for the foraminifera, is 9.974×10^4 , where B is 5×10^{-5} T, $T = 277.15$ K and k_B is 1.38×10^{-23} J/K.



Table S-3 The measurements of Fe isotope ratios in IRMM-014 standard using high resolution MC-ICP-MS. Uncertainty terms given are one relative standard deviation.

| Sample No. | $\delta^{56/54}\text{Fe}$ (‰) | 2 r.s.d. (‰) | $\delta^{57/54}\text{Fe}$ (‰) | 2 r.s.d. (‰) | Note |
|------------|-------------------------------|--------------|-------------------------------|--------------|---|
| 1 | 0.008 | 0.069 | 0.019 | 0.071 | Magnetite from environmental sediments after all the foraminifera were removed. |
| 2 | 0.139 | 0.052 | 0.217 | 0.060 | |
| 3 | -0.030 | 0.174 | -0.024 | 0.231 | Magnetite from foraminifera (<i>R. bilocularis</i>). |
| 4 | -0.046 | 0.169 | -0.053 | 0.229 | |



Supplementary Figures

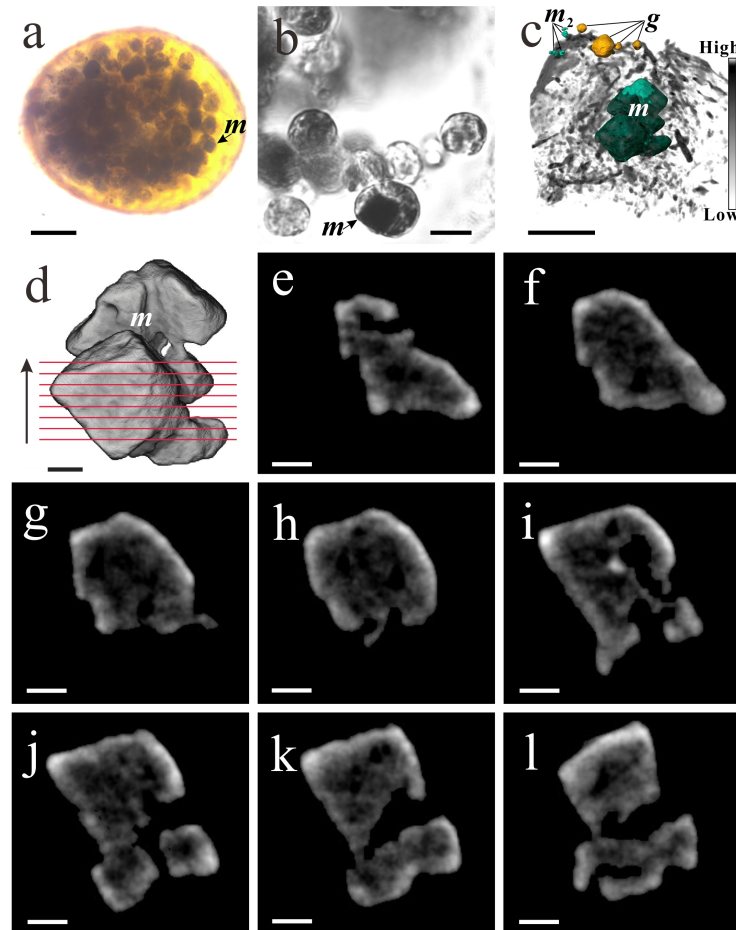


Figure S-1 Magnetite in foraminiferal stercomata. **(a)** Transmitted light image of magnetite inside the larger chamber of *R. bilocularis*. The magnetite is located within a stercome. **(b)** Confocal bright-field image of a localised *R. bilocularis*, with magnetite inside a stercome. **(c)** Phase contrast image of a stercome (red box range in Fig. 2a) based on synchrotron X-ray computerised tomography (NanoCT) analysis. The absorbance of the magnetite (*m*) in the foraminifera is similar to that of the standard magnetite (m_2), less than that of the gold particle (*g*). **(d)** 3D reconstructions from synchrotron X-ray computerised tomography of magnetite, the same particle as that marked as *m* in (c). The red lines show the positions of eight cross-sections from bottom to top of the particle in the direction of the arrow. **(e–l)** 3D reconstructions of the sections indicated by the red lines in (d). The sections have a spatial spacing of 0.296 μm . Each section shows the porous structure of magnetite with connections between the inside and outside. Magnetite in Figure S-1 is marked with *m* and arrow. Scale bars of a = 20 μm , b, c = 5 μm , d–l = 1 μm .

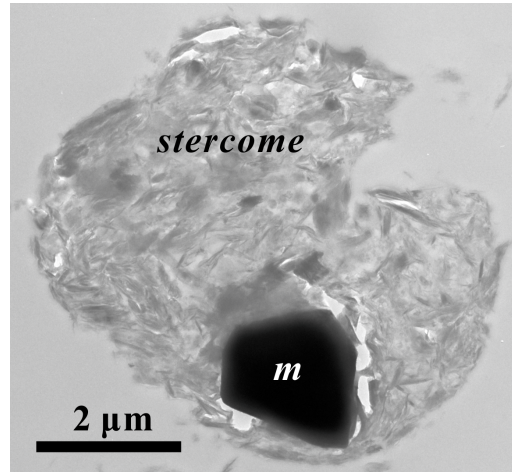


Figure S-2 TEM photomicrograph of magnetite (m) in a stercome of *R. bilocularis*.

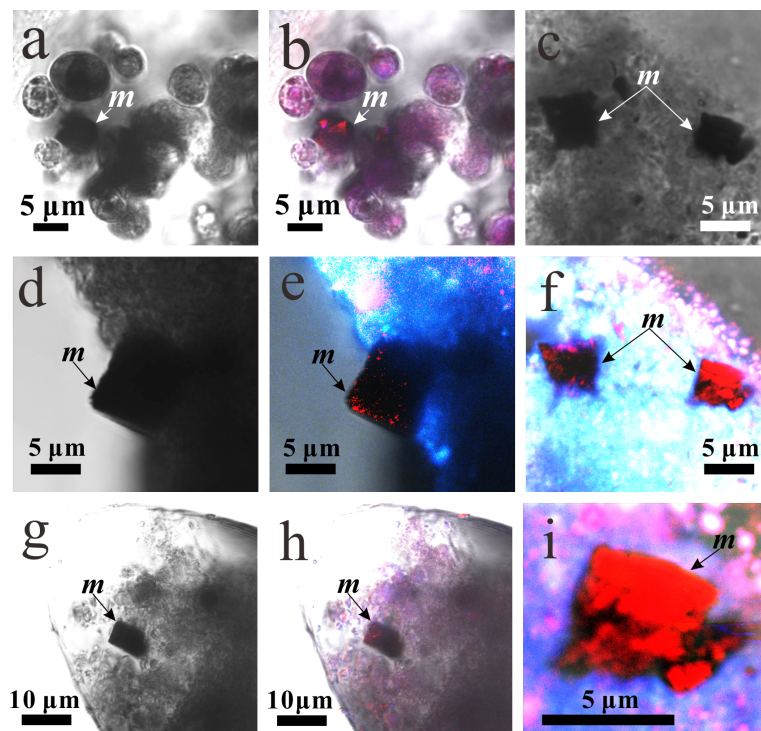


Figure S-3 Magnetite crystals inside *R. bilocularis* encapsulated by a lipid membrane. Magnetites are marked with an arrow and m. Lipids are stained red with Sudan IV. **(a)** Confocal bright-field photograph of the interior of *R. bilocularis*. Spherical structures are stercomata. **(b)** Composite image combining (a) and a laser confocal photograph of the same area after staining with Sudan IV. **(c, d)** Confocal bright-field images of the interior of *R. bilocularis* with stercomata that are partially decayed. **(e)** Composite image combining laser confocal images after DAPI, Sudan IV and phalloidin staining with bright field image. **(f)** Composite image combining laser confocal images after DAPI, Sudan IV and phalloidin staining with the bright field image. **(g)** Confocal bright-field image of the interior of *R. bilocularis* with stercomata that are partially decayed. **(h)** Composite image combining laser confocal image after Sudan IV staining with bright field image. **(i)** Enlarged image of the magnetite on the right side of (f).

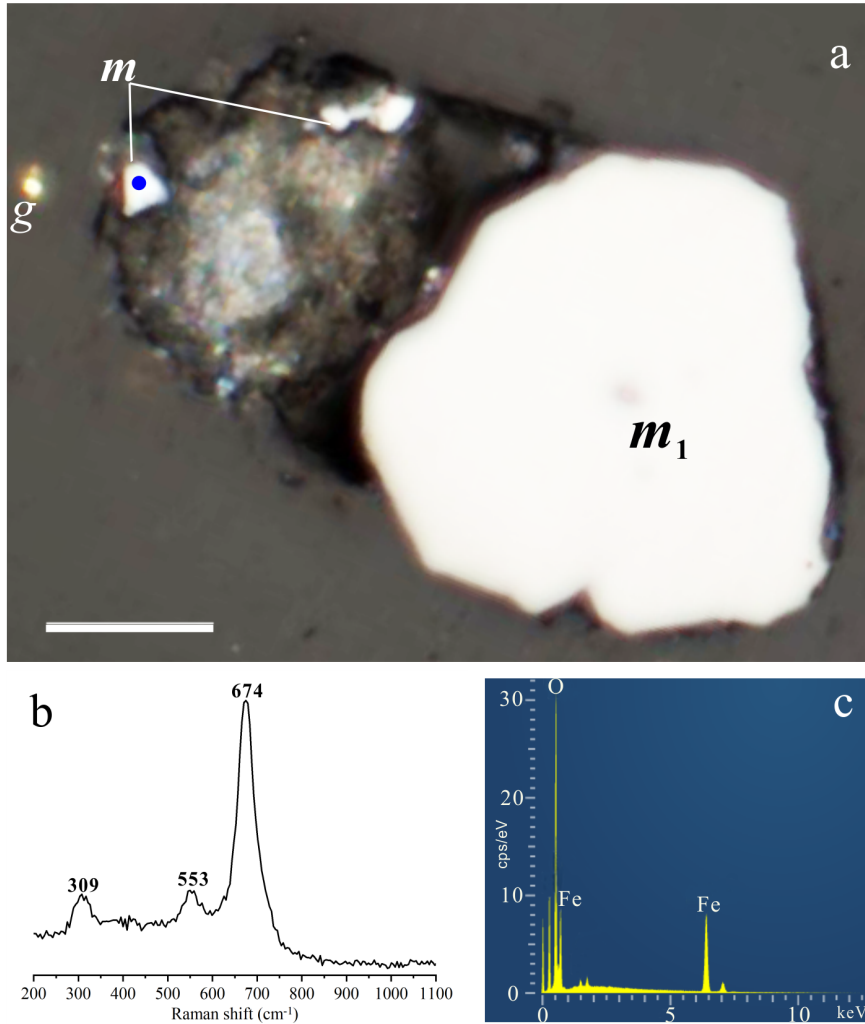


Figure S-4 Magnetite in a stercome of *R. bilocularis*. **(a)** Reflected light image of a foraminiferal stercome and standard sample (m_1) (blue box range in Fig. 1a), fixed with epoxy resin and polished with alumina powder. **(b)** The Raman spectrum corresponding to the blue points in (a). **(c)** SEM-EDX analysis of magnetite in foraminifera (white dot in Fig. 1b).

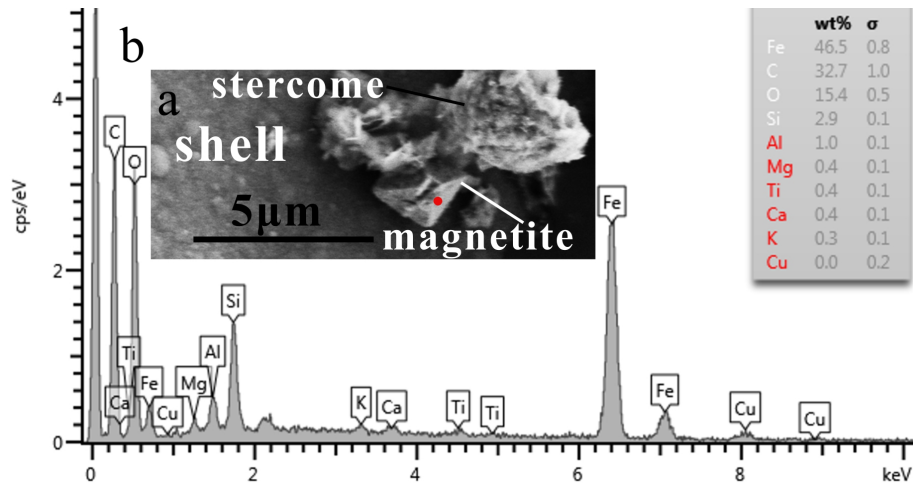


Figure S-5 SEM images of magnetite and stercome fragments of *R. bilocularis*. (a) Fragments of a disrupted stercome are distributed near the magnetite. (b) SEM-EDX analysis result for the location on the magnetite crystal marked by red dot in (a) showing the high carbon content associated with magnetite, possibly indicating the involvement of organic matter during the formation of magnetite.

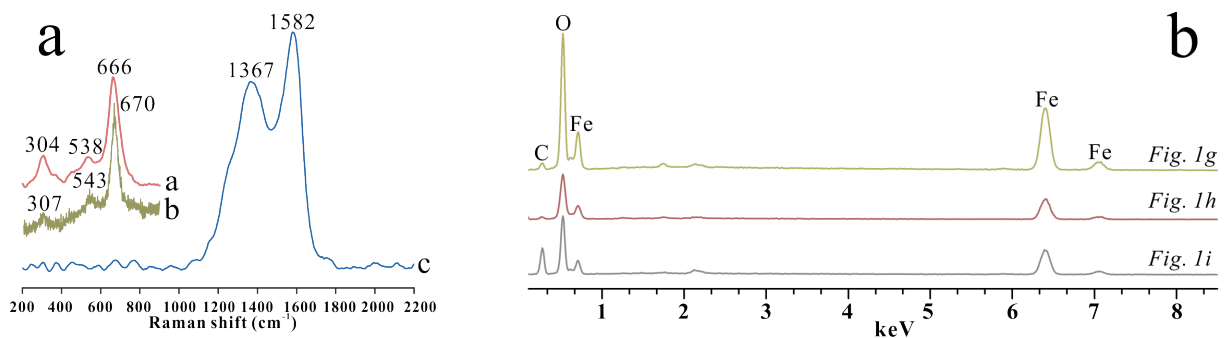


Figure S-6 Raman and SEM-EDX analysis of magnetite from *R. bilocularis*. (a) Representative Raman spectrum of magnetite and organic carbon used to obtain the Raman combined images in Figure 1f. (b) EDX spectra of magnetite particles marked with red points in Figure 1g–i. The Raman spectra of these magnetite particles are shown in Figure S-7b–d.

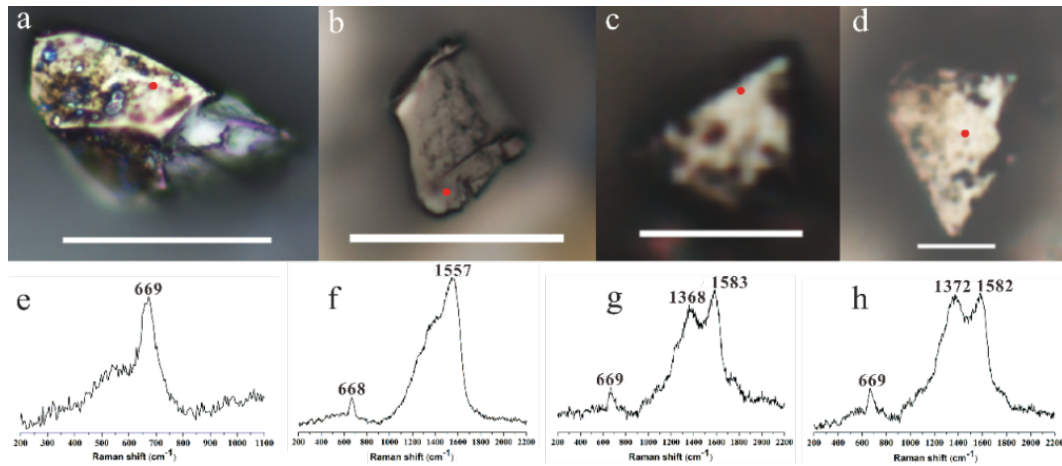


Figure S-7 Reflected light micrograph of magnetite from surrounding sediments and from foraminifera and corresponding Raman spectra. Raman analysis position is marked with a red dot. **(a)** Reflected light micrographs of magnetite in Figure S-8a from sediments. **(b)** Reflected light micrograph of FIB slice of magnetite in Figure 1i from foraminifera. **(c)** Reflected light micrograph of magnetite from foraminifera in Figure 1h. **(d)** Reflected light micrograph of magnetite with lipid membrane from foraminifera in Figure 1g. Scale bars for a = 40 μm , b = 20 μm , c = 4 μm and d = 4 μm .

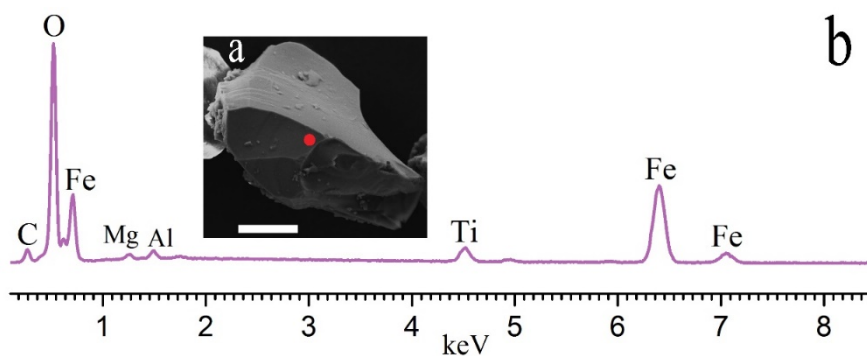


Figure S-8 SEM-EDX analysis of magnetite from surrounding sediments. **(a)** Secondary electron image of magnetite from sediments. **(b)** SEM-EDX spectrum at the location marked with red dot in (a). The Raman spectroscopy of this particle is shown in Figure S-7a. Scale bar of a = 20 μm .

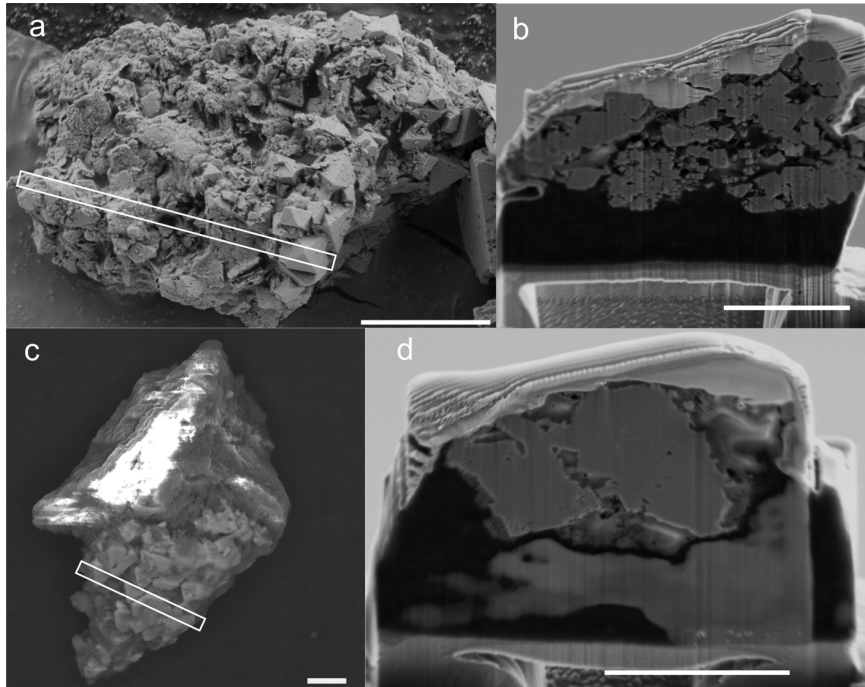


Figure S-9 SEM images of magnetite from the foraminifera *R. bilocularis* and the surrounding sediments. **(a)** SEM image of magnetite from *R. bilocularis* showing the location of FIB milled section (white rectangular). **(b)** FIB-SEM photomicrograph of magnetite area indicated in (a). **(c)** SEM image of magnetite from surrounding sediments showing the location of FIB milled section (white rectangular). **(d)** FIB-SEM photomicrograph of magnetite area indicated in (c). Scale bars of a = 10 μm , b–d = 5 μm .

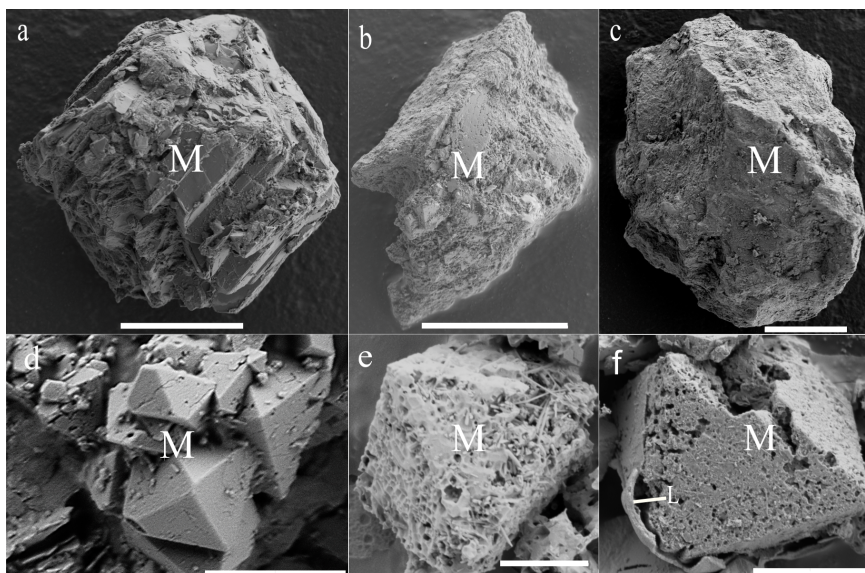


Figure S-10 Crystal morphology comparison of magnetite in environmental sediments with that in foraminifera. **(a–c)** Secondary electron image of magnetite (M) from environmental sediments. **(d–f)** Secondary electron image of magnetite (M) in *R. bilocularis*. P = Apatite; L = carbon-containing (lipid) membrane. Scale bars of a–c = 20 μm , others = 2 μm .

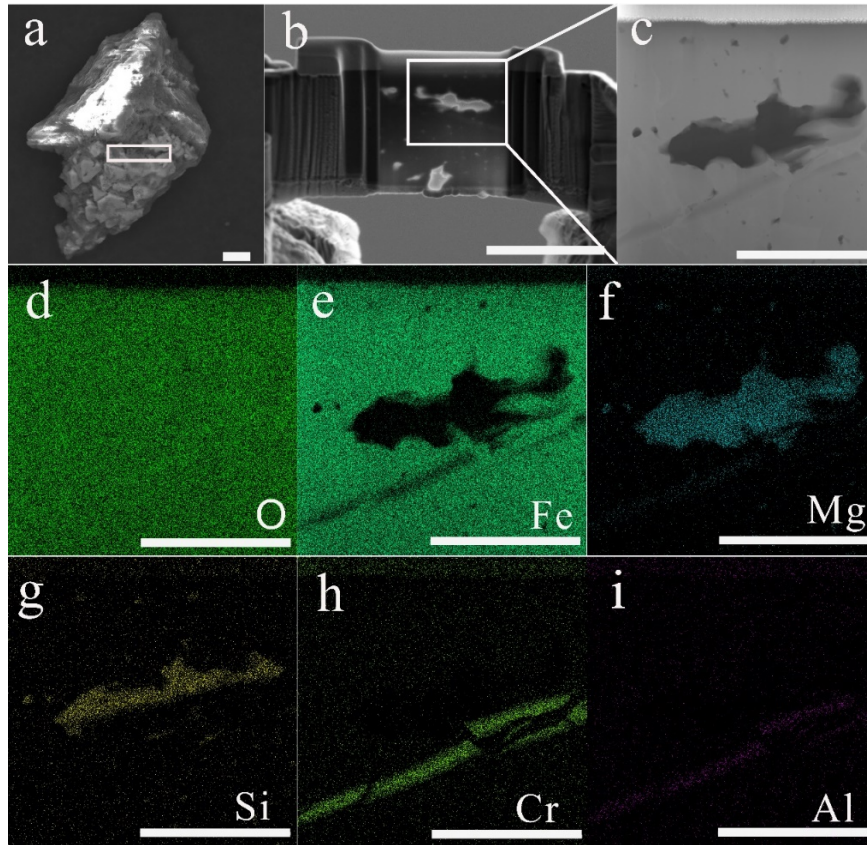


Figure S-11 Chemical composition of magnetite from surrounding sediments. **(a)** Backscatter electron (BSE) image of magnetite from sediments showing the location of FIB milled TEM section (white rectangular). **(b)** FIB-SEM photomicrograph showing inclusions in magnetite. **(c)** TEM photomicrographs of inclusions in magnetite. **(d–i)** TEM-EDS elemental maps showing the distribution of O, Fe, Mg, Si, Cr and Al in magnetite from sediments. Scale bars in a,b = 5 μm , others = 1 μm .

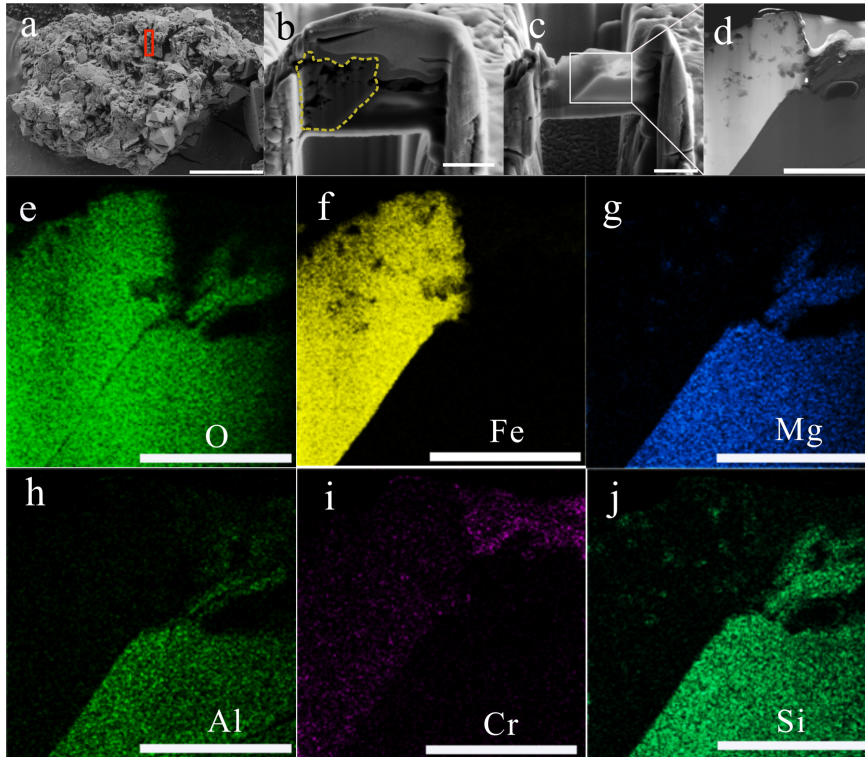


Figure S-12 Chemical composition of magnetite from the foraminifera *R. bilocularis*. **(a)** Backscatter electron (BSE) image of magnetite from *R. bilocularis* showing the location of FIB milled TEM lamella (red rectangular). **(b)** FIB-SEM photomicrograph showing the location of magnetite with yellow auxiliary line. **(c)** FIB-SEM photomicrograph of magnetite (TEM section of image b after FIB milling was performed). **(d)** TEM photomicrographs of magnetite (enlarged view of area in white rectangular of (c)). **(e–j)** TEM-EDS elemental maps showing the distribution of O, Fe, Mg, Al, Cr and Si in magnetite from *R. bilocularis*. Scale bars in a = 5 μm , others = 1 μm .

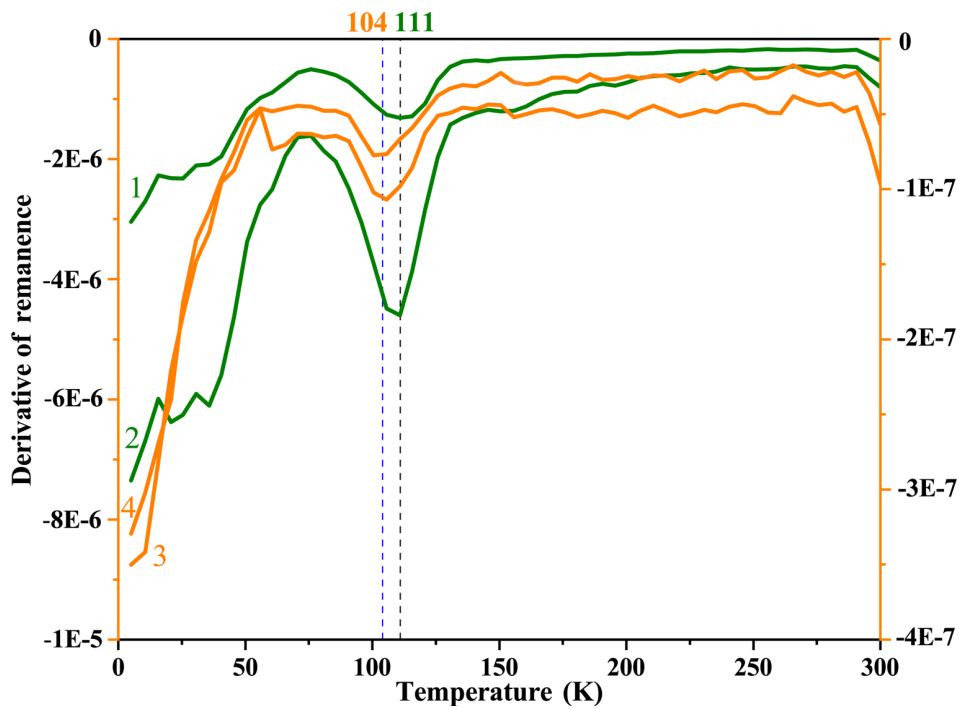


Figure S-13 Low-temperature magnetic properties of the magnetite from environmental sediments and foraminifera. The first-order derivative of the ZFC curves (1 and 2 indicate that the Verwey transition (T_V) temperature of magnetite from sediments peaks at 111 K; 3 and 4 indicate that the Verwey transition (T_V) temperature of magnetite from foraminifera peaks at 104 K). The ordinate is the first derivative of the total magnetic dipole moment of each sample, and the abscissa is the test temperature range of MPMS.

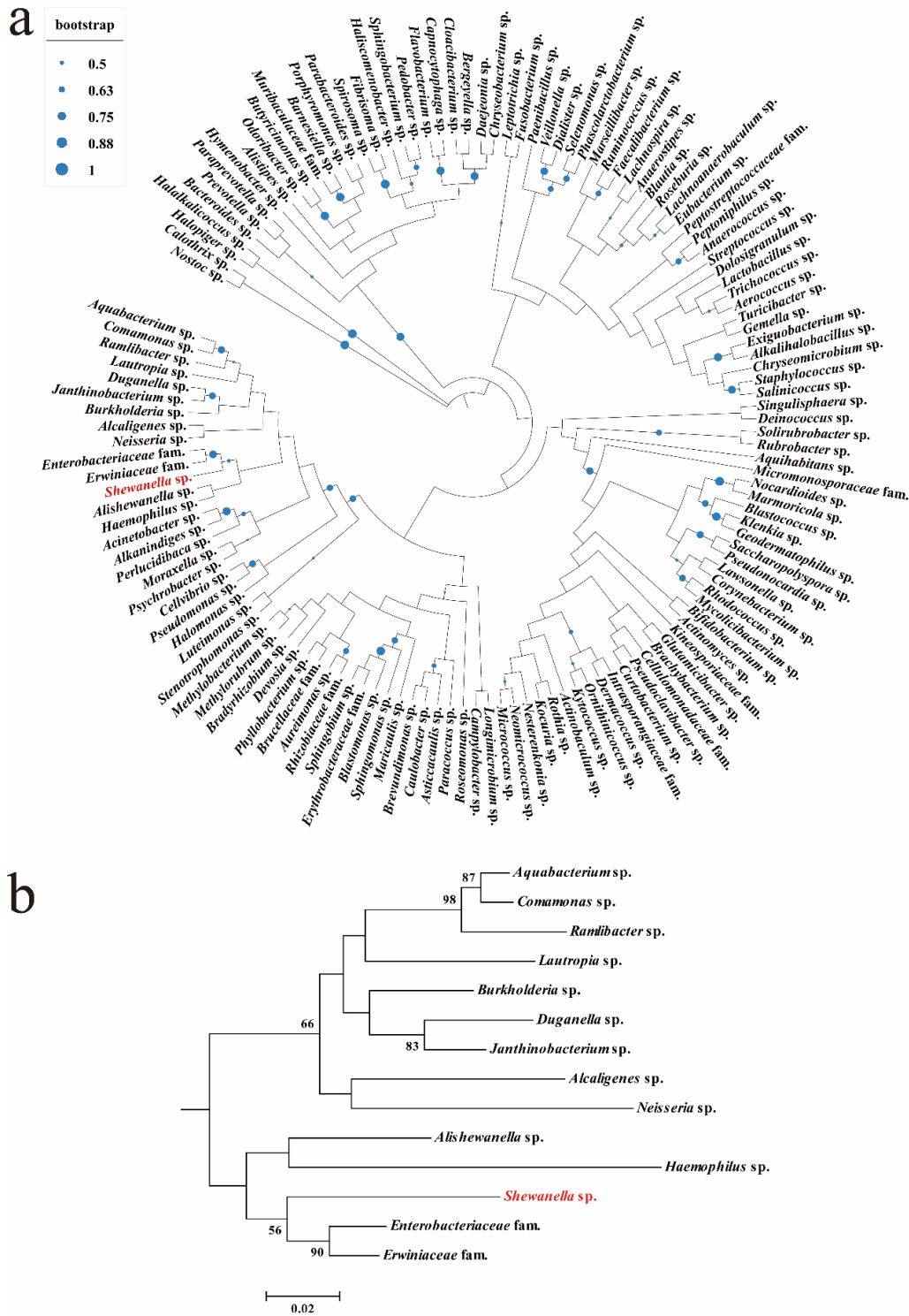


Figure S-14 Phylogenetic analysis of the internal bacteria within *Resigella bilocularis*. **(a)** Neighbour-joining phylogenetic tree based on 16S rRNA sequences that belong to the inner bacteria of *Resigella bilocularis*. **(b)** Subtree showing the position of *Shewanella* sp. and other species. Note: The dots (a) and the numbers (b) at branch nodes indicate bootstrap percentages derived from 1000 replications (only values above 50 % are shown). Scale bar of b = 0.02, substitution per nucleotide position.



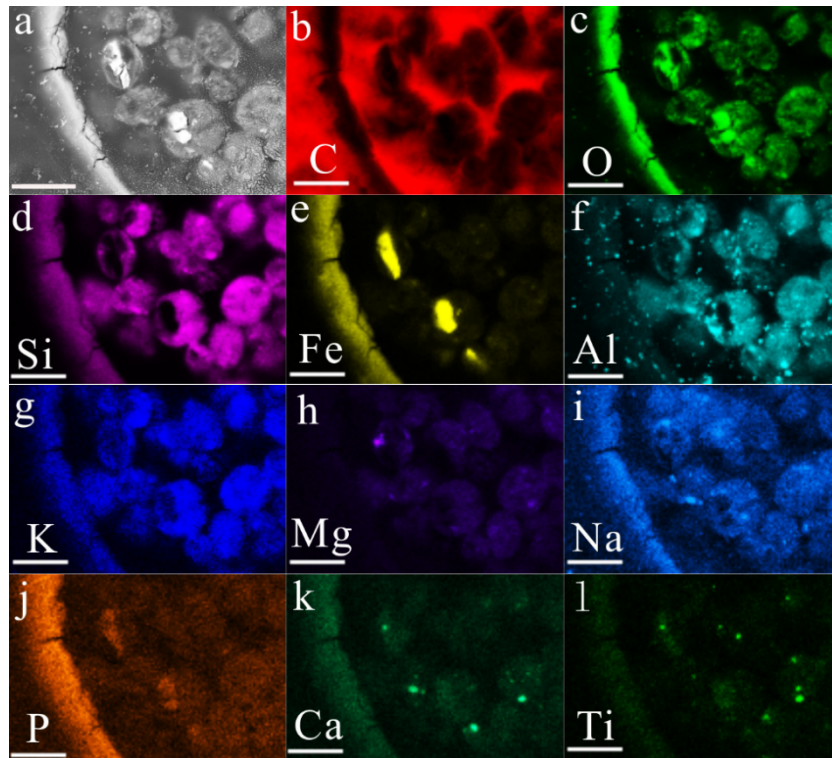


Figure S-15 Chemical composition of *R. bilocularis* analysed by SEM-EDX. (a) SEM image of foraminiferal slice at BSE model. (b–l) SEM-EDS elemental maps showing the distribution of C, O, Si, Fe, Al, K, Mg, Na, P, Ca and Ti, respectively. Scale bars = 10 µm.

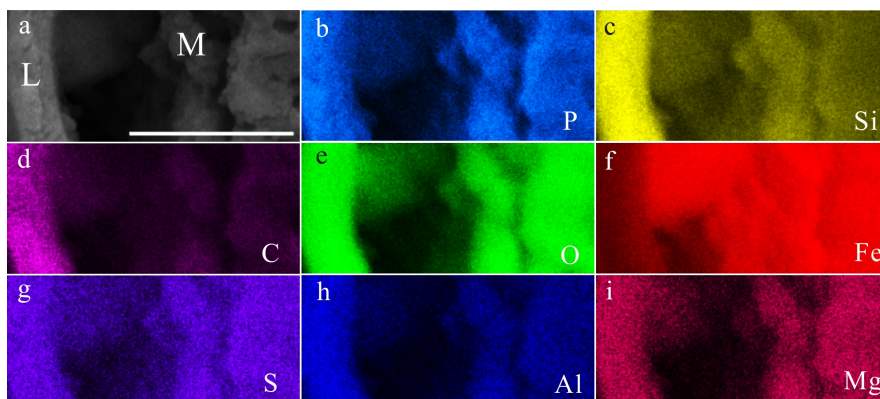


Figure S-16 Chemical composition of lipid membrane and enveloped magnetite. (a) SEM image of lipid membrane (L) and magnetite (M). (b–i) TEM-EDS elemental maps showing the distribution of P, Si, C, O, Fe, S, Al and Mg, respectively. Note that P and C are enriched not only in the lipid membrane, but also magnetite, suggesting that the magnetite has a biological origin. Scale bar = 10 µm.

Supplementary Videos

Video S-1 Movie showing the response of *R. bilocularis* from the Mariana Trench to varying external magnetic fields, recorded by a Leica M205C stereo microscope.

Video S-2 Movie of hard X-ray synchrotron 3D reconstructions of individual stercomata of *R. bilocularis* containing scattered magnetite crystals.

Videos S-1 and S-2 can be downloaded (.mov) at <https://doi.org/10.7185/geochemlet.2212>.

Supplementary Information References

- Amor, M., Busigny, V., Durand-Dubief, M., Tharaud, M., Ona-Nguema, G., Gélabert, A., Alphantery, E., Menguy, N., Benedetti, M.F., Chebbi, I., Guyot, F. (2015) Chemical signature of magnetotactic bacteria. *Proceedings of the National Academy of Sciences* 112, 1699–1703. <https://doi.org/10.1073/pnas.1414112112>
- Bernhard, J.M., Ostermann, D.R., Williams, D.S., Blanks, J.K. (2006) Comparison of two methods to identify live benthic foraminifera: A test between Rose Bengal and CellTracker Green with implications for stable isotope paleoreconstructions. *Paleoceanography* 21, 4210–4218. <https://doi.org/10.1029/2006PA001290>
- Blakemore, R.P., Frankel, R.B. (1981) Magnetic navigation in bacteria. *Scientific American* 245, 58–65. <https://doi.org/10.1038/scientificamerican1281-58>
- Gao, P., Sun, X.X., Xiao, E.Z., Xu, Z.X., Li, B.Q., Sun, W.M. (2019) Characterization of iron-metabolizing communities in soils contaminated by acid mine drainage from an abandoned coal mine in Southwest China. *Environmental Science and Pollution Research* 26, 9585–9598. <https://doi.org/10.1007/s11356-019-04336-6>
- Lins, U., Bazylinski, D.A. (2009) Magnetotaxis. In Johnson, G.J. (Ed.) *Encyclopedia of Microbiology*. Emerald Publishing Limited, Bingley, 229–241. <https://doi.org/10.1016/B978-012373944-5.00103-6>
- Malinovsky, D., Stenberg, A., Rodushkin, I., Andren, H., Ingri, J., Öhlander, B., Baxter, D.C. (2003) Performance of high resolution MC-ICP-MS for Fe isotope ratio measurements in sedimentary geological materials. *Journal of Analytical Atomic Spectrometry* 18, 687–695. <https://doi.org/10.1039/B302312E>
- Murray, J.W., Bowser, S.S. (2000) Mortality, protoplasm decay rate, and reliability of staining techniques to recognize ‘living’ foraminifera: a review. *Journal of Foraminiferal Research* 30, 66–70. <https://doi.org/10.2113/0300066>

